QUARTERLY JOURNAL
OF THE
ROYAL METEOROLOGICAL SOCIETY

Vol. 129 OCTOBER 2003 Part A No. 594

Q. J. R. Meteorol. Soc. (2003), **129**, pp. 2847–2866 doi: 10.1256/qj.02.166

Bimodality in tropical water vapour

By CHIDONG ZHANG[1]*, BRIAN E. MAPES[2] and BRIAN J. SODEN[3]

[1]*Rosenstiel School of Marine and Atmospheric Science, University of Miami, USA*
[2]*CIRES/NOAA Climate Diagnostics Center, Boulder, USA*
[3]*NOAA Geophysical Fluid Dynamics Laboratory, Princeton, USA*

(Received 5 August 2002; revised 17 March 2003)

SUMMARY

Probability distribution functions of tropospheric water vapour in the tropics are shown to be commonly bimodal. This bimodality implies sharp gradients between dry and moist regimes in space and time. A method of testing for and quantifying bimodality is introduced. Using this method, the bimodality of water vapour is surveyed in satellite and *in situ* observations, as well as in global model re-analysis data and simulations. The bimodality suggests that the radiative drying time after an injection of moisture by convection is short (1–2 days) compared to a homogenizing time, whether physical (mixing) or mathematical (averaging). It is shown that the local bimodality found in cloud-model simulations and *in situ* point measurements disappears with modest time averaging (18 h and 200 km), but then reappears on the global-scale, where dry and moist regions are separated so widely that synoptic- and large-scale mixing times exceed the drying time-scale. Large discrepancies exist in the ability to reproduce the global-scale bimodality by global model re-analysis and simulations.

KEYWORDS: Humidity Mixing Probability distribution function

1. INTRODUCTION

Water vapour plays a key role in governing the flow of energy within the earth's climate. It is the dominant greenhouse gas, helps regulate the formation and dissipation of clouds and, when changing phase, provides a key source or sink of latent heat. Because its concentration depends strongly upon temperature, water vapour also provides an important feedback mechanism for the climate system. Indeed, water-vapour feedback is widely considered to provide the largest known mechanism for amplifying both future (IPCC 2000 and references therein) and past (Broecker 1997) climate changes. Of the total feedback from water vapour, current climate models predict that roughly two-thirds originates from the upper troposphere (Held and Soden 2000). Although the fidelity of model predictions of water-vapour feedback, particularly in the upper troposphere, has been debated for more than a decade, the balance of evidence suggests that water vapour provides a strong positive feedback consistent with that predicted by current models (IPCC 2001).

Aside from its effects on the global-mean radiation balance, water vapour plays a vital role in the general circulation. This is especially true in the tropics, where the moisture field exerts strong influence over both halves of the (spatially inhomogeneous)

* Corresponding author: 4600 Rickenbacker Causeway, MPO, Miami, Florida 33149-1098, USA.
e-mail: czhang@rsmas.miami.edu

radiative–convective energy balance which characterizes the heat budget. For example, long-wave cooling by water vapour necessitates mean subsiding motion over large areas of the tropics. This downward motion in turn tends to dry the air, closing an important radiative–dynamical feedback loop. At the same time, lower- and middle-tropospheric moisture is an important precursor for moist convection (Sherwood 1999; Tompkins 2001), quite possibly with a steep or threshold-like nonlinear dependence. Convection in turn acts to shape the humidity field, through mixing, precipitation, transport, condensation, and heating-induced circulations. The effects of humidity variations on radiation and convection are also active in dynamic variability on synoptic and smaller scales (Mapes and Zuidema 1996; Yoneyama and Parsons 1999). Even beyond its importance to radiative and convective heating processes, water vapour is of interest as a tracer of atmospheric convection and circulation. For example, there is an extensive literature on dynamical deductions springing from observations of the low water-vapour mixing ratio in the tropical lower stratosphere (e.g. 'stratospheric fountain' of Newell and Gould-Stewart (1981) and 'stratospheric drain' of Sherwood (2000)).

This paper reports our attempt to document, and to consider what can be deduced from, observations of bimodal probability distribution functions (PDFs) of tropospheric water vapour. In the tracer framework, the importance of bimodality lies in its physical interpretation. Is it a trivial or unsurprising consequence of the two physical limits on the range of allowed humidity (zero and saturation)? Or, is it an informative and discriminating diagnostic of moist circulations? Perhaps the simplest system possessing a bimodal distribution is a monochromatic wave in one dimension (sine curve). For example, the mean annual time series of middle-latitude surface temperature, being dominated by the annual harmonic, exhibits a bimodal PDF. However, this trivial case of a one-dimensional sinusoid is easily spotted by visual inspection of the time series, and is not the explanation for any bimodal PDFs discussed in this study. The PDF of a two-dimensional sinusoidal surface (peaks and valleys) is unimodal. Not every sum of two Gaussian distributions with different means is bimodal, so even the physical coexistence of distinct dry and moist regimes is not sufficient to guarantee a bimodal PDF. The key aspect of a significantly bimodal distribution is the abruptness of the boundary between the dry and moist regimes. This suggests that mixing between high- and low-humidity air masses is slow compared to the time-scales involved in their production.

Soden and Bretherton (1993) showed that for regions over the eastern Pacific and the Atlantic Oceans (0–150°W, 60°N–60°S), the PDF of cloud-free upper-tropospheric relative humidity (RH), retrieved from satellite remote sensing data, is approximately log-normal. They interpreted this in terms of isentropic vertical displacement of air parcels by vertical velocities that are normally distributed in an atmosphere with a constant RH and lapse rate. Yang and Pierrehumbert (1994) found that PDFs of total-sky upper-tropospheric water vapour in middle latitudes are bimodal. One peak represents near-saturated air parcels that originated in the tropics, while the other represents dry air parcels subsiding along isentropic surfaces from higher latitudes. The interpretation of bimodality in that case is that filaments of air with different origins are transported long distances in the meridional direction before mixing destroys their identity.

Bimodal PDFs have also been found for water vapour in the tropics. Brown and Zhang (1997) found that the PDF of upper-tropospheric RH in a large set of soundings in the equatorial western Pacific was bimodal. This study is an extension of their finding to several other datasets on various space- and time-scales, and an attempt at deducing physical meaning from the observations. Section 2 describes the datasets used in this study. Section 3 introduces an objective test for bimodality, as well as some summary parameters developed from a two-Gaussian fit. Section 4 examines *in situ* and isotropic

TABLE 1. SUMMARY OF DATA

Dataset[1]	Location	Instrument/platform	Resolution	Time
TOGA COARE	Western Pacific	rawinsondes	6 h/5 hPa	November 1992–February 1993
CEPEX	Central Pacific	dropsondes	10 hPa	4 March–6 April 1993
TEPPS	7.8°N, 125°W	rawinsondes	4 h/10 hPa	8–24 August 1997
JASMINE	Indian Ocean	rawinsondes	3 h/5 hPa	May 1999
FGGE	Eastern Pacific	dropsondes	10 hPa	January–February 1979
ARM	147.4°E, 2.1°S	rawinsondes	daily/5 hPa	January–March 2001
EPIC	95°W, 0–12°N	aircraft probes	120–180 m	5 September–10 October 2001
NVAP	Tropics	rawinsondes, satellite (microwave, infrared)	monthly/1° × 1° three layers	January 1988–December 1997
SSMR	Tropical oceans	satellite (microwave)	monthly/1° × 1° vertical column	January 1979–December 1984

[1] See text for translation of acronyms.

cloud-resolving model data, discovering evidence for bimodality at these small scales. This leads into section 5, which interprets bimodality in terms of the relative time-scales for drying and mixing processes. Section 6 extends the inquiry to global-scale climatological bimodality, in the spatial distributions of upper-tropospheric humidity for various seasons. Section 7 gives a concluding discussion.

2. DATA

A number of datasets are used in this study to demonstrate that the bimodality in water vapour exists, independently of observational platforms, in different regions in the tropics. There are generally three types of data: *in situ* soundings, including land- and ship-based upper-air soundings and aircraft dropsondes; *in situ* aircraft flight-level measurement; and remotely sensed data from satellites. Most of the *in situ* sounding data are from special field campaigns. The remote-sensing data are from different satellites and different instruments. One dataset is a combination of *in situ* and satellite products. These data can be categorized as repeated sampling at fixed locations (typically for land/ship-based upper-air soundings and satellite remote-sensing retrievals), and random sampling in time and space (typically for ship-based soundings and aircraft measurements). A summary of the data is given in Table 1.

(*a*) *TOGA COARE*

Upper-air soundings were collected from land- and ship-based sites in the equatorial western Pacific from November 1992 to February 1993, the Intensive Observation Period of the Tropical Ocean Global Atmosphere Coupled Ocean-Atmosphere Response Experiment (TOGA COARE, Webster and Lukas 1992). Used in this study are 2900 soundings from the Intensive Flux Array (see Brown and Zhang 1997). The data were collected four times a day; the vertical resolution is 5 hPa. Issues related to the quality of the data have been discussed by Wang *et al.* (2002). The totality of this dataset sampled variability in both space and time.

(*b*) *TEPPS*

Upper-air soundings were collected six times a days at 7.8°N, 125°W for 16 days (8–23 August 1997) during the Tropical Eastern Pacific Process Study (TEPPS, Yuter and Houze 2000). The vertical resolutions of the soundings from two types of sonde models are 30 and 300 m, which were binned into a dataset with resolution 10 hPa.

This dataset (95 soundings) sampled variability in time during a month in a strong intertropical convergence zone (ITCZ) in the eastern Pacific.

(*c*) *JASMINE*

During the Joint Air–Sea Monsoon Interaction Experiment (JASMINE, Webster *et al.* 2002), upper-air soundings were launched from two research vessels cruising north and south (15°N–5°S) near 89°E during May 1999. This dataset (207 soundings of 5 hPa vertical resolution) sampled variability in both time and space (latitude).

(*d*) *ARM*

Upper-air sounding data are collected from Manus (147.4°E, 2.1°S), a western Pacific site of the Atmospheric Radiation Measurement (ARM) Program (Mather *et al.* 1998). Soundings are carried out once or twice daily, with typical vertical resolutions of 1.0–1.5 hPa. A subset of these data, including 103 soundings of 5 hPa vertical resolution collected during January–March 2001, is used in this study.

(*e*) *CEPEX*

During the Central Equatorial Pacific Experiment (CEPEX, Lohmann *et al.* 1995), dropsondes were launched from an aircraft repeatedly flying an irregular pattern between 4 March and 6 April 1993 in a region within 2°N–18°S and 160°E–170°W. The original vertical resolution is about 5 hPa and is reduced to 10 hPa. This dataset (92 soundings) can be considered as a random sample with respect to weather events, in an area deliberately chosen because sharp gradients in cloud and water vapour were anticipated (Kley *et al.* 1997).

(*f*) *FGGE*

During the First Global Atmospheric Research Program Global Experiment (FGGE), aircraft dropsonde data were collected in the area, 15°N–15°S, 90°–160°W, in two observation periods: January–February and May–June 1979 (Kloesel and Albrecht 1989). The vertical resolution of the data is 10 hPa. Because of the irregular timing and location for these dropsondes (see Fig. 2 in Yin and Albrecht 2000), they can be considered to be randomly sampling the atmosphere in both time and space over the eastern Pacific ITCZ and cold tongue. In this study, only the dropsondes (250) within and near the ITCZ (5–10°N) during the first observation period (January–February) are used.

(*g*) *EPIC2001*

Water vapour was measured by instruments aboard an aircraft during the Eastern Pacific Investigation of Climate 2001 field campaign (EPIC2001, Weller 1999), which took place from 5 September to 10 October 2001. The flight pattern started from the equator, typically at 1900 UTC, and continued at a constant altitude of 5500 m to 12°N along 95°W within about 2–3 hours. The same pattern was repeated eight times. The distribution of the flight data is essentially fixed in space but random in time. The resolution of the measurement is 1 s, or roughly 120–180 m.

(*h*) *NVAP*

The dataset of the NASA (National Aeronautics and Space Administration) Water Vapor Project (NVAP, Randel *et al.* 1996) is a combination of water-vapour measurements from conventional upper-air soundings and from satellite infrared/microwave observations. The NVAP products used in this study are monthly means of gridded ($1^\circ \times 1^\circ$) precipitable water (PW) for three layers (surface–700 hPa, 700–500 hPa, and 500–300 hPa) and the total atmospheric column. The dataset covers 1988–97. Possible biases in this dataset may come from non-uniform distributions of the data sources (soundings over land areas and satellite over oceans) and procedures of substituting for missing data. These concerns will be briefly addressed later.

(*i*) *SSMR*

Column integrated PW retrieved from the Special Sensor Microwave Radiometer (SSMR) microwave (10 GHz) channel is available from 1979 to 1984 inclusive (Bates and Jackson 1997). Climatological monthly mean PW ($1^\circ \times 1^\circ$) is used in this study.

In addition to these water vapour data, precipitation (Xie and Arkin 1997), outgoing long-wave radiation (OLR, Liebmann and Smith 1996), and the Special Sensor Microwave/Imager (SSM/I) cloud liquid path (Weng and Grody 1994) are also used. Output from numerical models, including a cloud-resolving model, a global climate model, and a global model re-analysis product are also examined.

3. Bimodality test and indices

To explore the characteristics of bimodality objectively, a formal test of its statistical significance and quantitative measures of its strength are needed. In some methods of testing for bimodality, parameters have to be specified a priori. In this study, we apply a non-parametric significance test for unimodality, in combination with visual inspection to determine whether non-unimodal PDFs are in fact bimodal.

For a given dataset, a null hypothesis H_0 is made that its PDF is unimodal. A 'dip test' for unimodality (Hartigan 1985; Hartigan and Hartigan 1985) is performed to test H_0 (see appendix). When hypothesis H_0 is rejected at the confidence level of 95%, bimodality is confirmed if two and only two obvious peaks are seen in the estimated PDF. Equivalently, if two peaks are first seen in an estimated PDF, then bimodality is confirmed only if H_0 is rejected by the dip test. The existence of bimodality, therefore, depends on both rejecting H_0 and the existence of two unambiguous peaks in the estimated PDF. In practice, this appears to be a conservative way to identify bimodality. In many cases, two peaks can be discerned in estimated PDFs but H_0 cannot be rejected by the dip test. Yet, this is an imperfect way of detecting bimodality. Rejecting H_0 only confirms multimodality but not necessarily bimodality. In this study, all cases where bimodality is considered to exist satisfy the criterion without any ambiguity as to whether there are two or more modes.

When bimodality is confirmed, it is quantified by measuring the amplitude and separation of the two peaks. A mixture of two normal functions is used to best fit an estimated PDF; this choice is purely for simplicity (Reschenhofer 2001). A histogram is used to estimate the PDF from a given dataset. The number of bins is chosen to equal the square root of the sample points (Panofsky and Brier 1958). The bimodal normal mixture is expressed as:

$$F_{\mathrm{B}}(x) = A_1 \exp\{(x - \mu_1)^2/2\sigma_1^2\} + A_2 \exp\{(x\mu_2)^2/2\sigma_2^2\}, \quad (1)$$

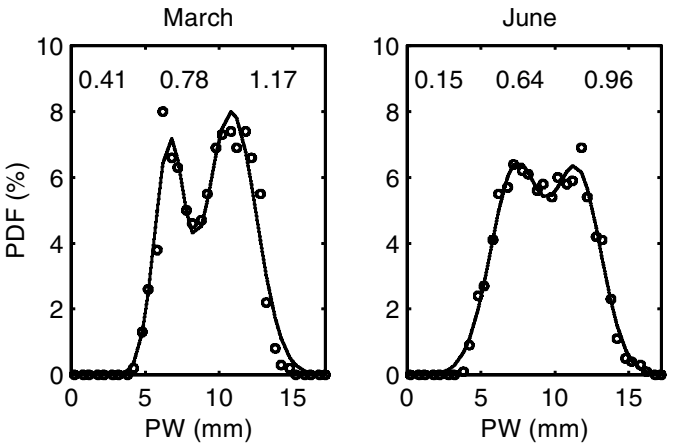

Figure 1. Estimated probability density functions (PDFs) of climatological mean precipitable water (PW) for March and June based on NASA Water Vapor Project data (circles) and their best fit by normal mixtures (solid lines). The numbers listed near the top of each panel are values of, from left, bimodal amplitude A_B, bimodal separation S, and bimodal ratio R.

where six parameters must be determined by the fitting of amplitudes, A_i, means, μ_i, and standard deviations, σ_i, where $i = 1$ or 2. Once $F_B(x)$ is fitted to a bimodal PDF, the bimodality can be quantified by three quantities. One is 'bimodal amplitude':

$$A_B = \Delta A / A_M, \tag{2}$$

where $\Delta A = A_M - A_V$ with A_V being the amplitude of the minimum PDF between the two peaks and A_M the amplitude of the smaller peak of the two. The existence of the smaller peak is essential for a bimodal distribution, while the larger peak is taken for granted as from the normal Gaussian distribution. For any given bimodal PDF, $A_B < 1$; a larger A_B indicates more distinct double peaks. A_B approaches unity as the overlap between the two peaks approaches zero. Another quantity is 'bimodal separation':

$$S = (\mu_2 - \mu_1)/(2\sigma_1 + 2\sigma_2), \tag{3}$$

where $\mu_2 > \mu_1$. S measures the distance between the means of the two normal functions, which is roughly the distance between the two peaks. $S > 1$ only if the two normal functions essentially do not overlap. The third quantity is 'bimodal ratio':

$$R = A_r / A_L, \tag{4}$$

where A_r and A_L are the amplitudes of the right and left peaks, respectively. This quantity indicates which of the two peaks dominates.

For water vapour, A_B measures the effectiveness of mixing effects of the atmosphere; a large A_B indicates weaker mixing (or mixing time-scales much longer than drying time-scales, see section 5). S measures the gradient between the dry and moist modes; a large S indicates a coexistence of dry and moist regimes in a confined domain (in time and/or space). R indicates whether the bimodality occurs in a dominating moist ($R > 1$) or dry ($R < 1$) regime. A distinct bimodality in water vapour corresponds to both a large A_B and S, implying a large separation between a source (precipitating) region and one where effective drying mechanisms, strong subsidence and/or lateral advection (Zhang and Chou 1999) are at work, with little mixing in between.

Examples of the fittings are plotted in Fig. 1 to illustrate the utility of these quantities. Estimated PDFs (histograms) of NVAP mid-tropospheric (500–300 hPa) PW for 20°N–20°S are plotted as open circles for climatological means in March and June. Best fits of the Gaussian mixture are solid lines. Near the top of each panel, the corresponding values of A_B, S, and R are listed from the left to right. The dip test rejects H_0 for both months. The bimodal signature appears more prominent for March than June; this is quantitatively measured by A_B, which is 0.41 for March and only 0.15 for June. The bimodal separation S is comparable for the two months. The bimodal ratio R for these two examples presents an interesting case: the maximum of the estimated PDF corresponds to the dry mode in March but to the moist mode in June; but the bimodal ratio defined above indicates that the moist mode dominates in March whereas the dry mode does slightly in June. These discrepancies arise from the abnormally large amplitude of a single bin in each estimated PDF. Without that, the visual impression of the dominant mode as a whole would be consistent with the measured R. Physically, it is conceivable that a moist regime dominates in March when deep moist convection, which is the main source of water vapour in the troposphere, is more concentrated in the tropics, while in June a dry regime may dominate the tropics when deep convection partially migrates out of the tropical latitudes as part of the global annual cycle.

In general, not all estimated PDFs with two peaks can be declared bimodal according to the dip test. It is also true that when H_0 fails to be rejected, bimodal amplitudes, when there are two peaks, are usually very small. Bimodal separation and ratio did not appear to give any indication as to whether H_0 would be rejected. A combination of the dip test, visual inspection of estimated PDFs, and the bimodal indices serves as a conservative and sufficient way of identifying and quantifying bimodality.

4. Small-scale bimodality and process interpretation

Figure 2 shows vertically resolved histograms of Δq (deviation of specific humidity from its mean) for sounding data from various tropical regions. This figure demonstrates that the bimodality in water vapour exists in the middle to upper troposphere (500–200 hPa) of different tropical climate regimes, including the Indian summer monsoon (JASMINE), the western Pacific warm pool (TOGA COARE, ARM), the edge of the warm pool in the central Pacific (CEPEX), and the eastern Pacific ITCZ (TEPPS, FGGE). Apparently, processes leading to a bimodal distribution are already active in the scales of day-to-day convective and synoptic weather variations passing over the sounding sites, of which most of these soundings form a set of essentially random point samples. It is noticed that at least two of the datasets shown in Fig. 2 (FGGE and CEPEX) might suffer from an inability to measure RH accurately below 20%.

Aircraft data (Fig. 3) give a view of middle-tropospheric humidity variations with spatial continuity and more accuracy. A block-like or 'blocky' structure is seen on scales of 10–100 km, with values near saturation in some regions and much lower in others. The transition zones with intermediate humidity values are narrow, which leads to a bimodal PDF (Fig. 4). Presumably, this blocky structure in one-dimensional transects reflects filamentary structure in two dimensions, with tongues of moist and dry air intertwined but not mixed. Similar blocky structure can also be seen in some cases in COARE aircraft data we have examined (not shown). Cho *et al.* (2000) showed that scaling laws fit blocky aircraft-measured humidity reasonably well across a wide range of scales.

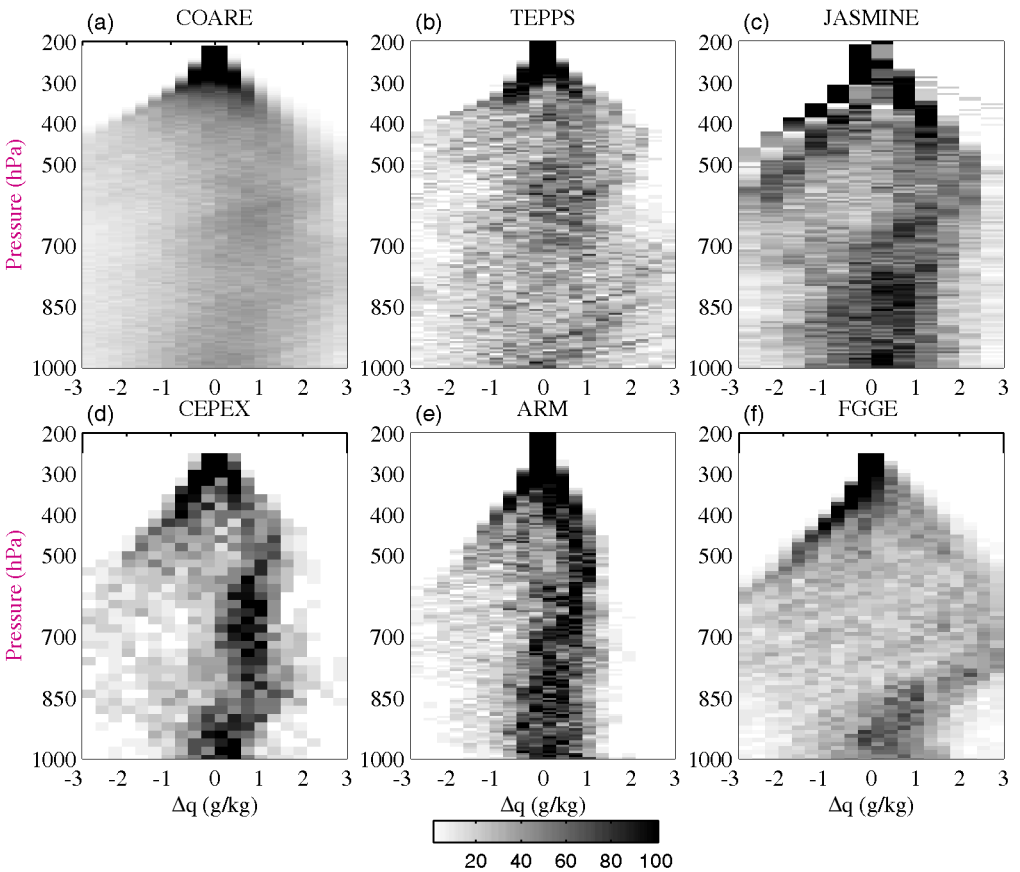

Figure 2. Estimated probability density function of the deviation of specific humidity, Δq, from its time average, based on (a) 2900 TOGA COARE soundings, (b) 95 TEPPS soundings, (c) 207 JASMINE soundings, (d) 92 CEPEX dropsondes, (e) 103 ARM soundings, and (f) 250 FGGE dropsondes. See section 2 for translation of acronyms.

A full two-dimensional view of humidity at a similarly fine resolution can at present only be obtained from models. Figure 5 shows the humidity field at 10 km altitude in a 'snapshot' from the cloud-resolving model data of Tompkins (2001). This snapshot is profoundly representative, since the spatial domain is isotropic, homogeneous, and doubly periodic, and this is an arbitrary time-slice in a statistically steady radiative–convective equilibrium. There is no imposed mean wind shear. Two circular convective cores of ~3 km diameter can be seen in the upper-left quadrant, while other patches of lesser but still high humidity can be seen, many curled within eddies of scales ~5–10 km.

The PDF of values in Fig. 5 is shown in Fig. 6, and is clearly bimodal. The humidity value with minimum frequency (352×10^{-6} kg kg^{-1}) is indicated in Fig. 5 by a dashed line. Dry patches, in which humidity is lower than this value, can be seen to occur with scales exceeding 20 km. In this model run the lower boundary is uniform, so all spatial structures are internally determined by convection. In fact, the humidity field itself is a major creator of structure in the convection, which in turn structures the humidity field (explored more thoroughly in Tompkins 2001).

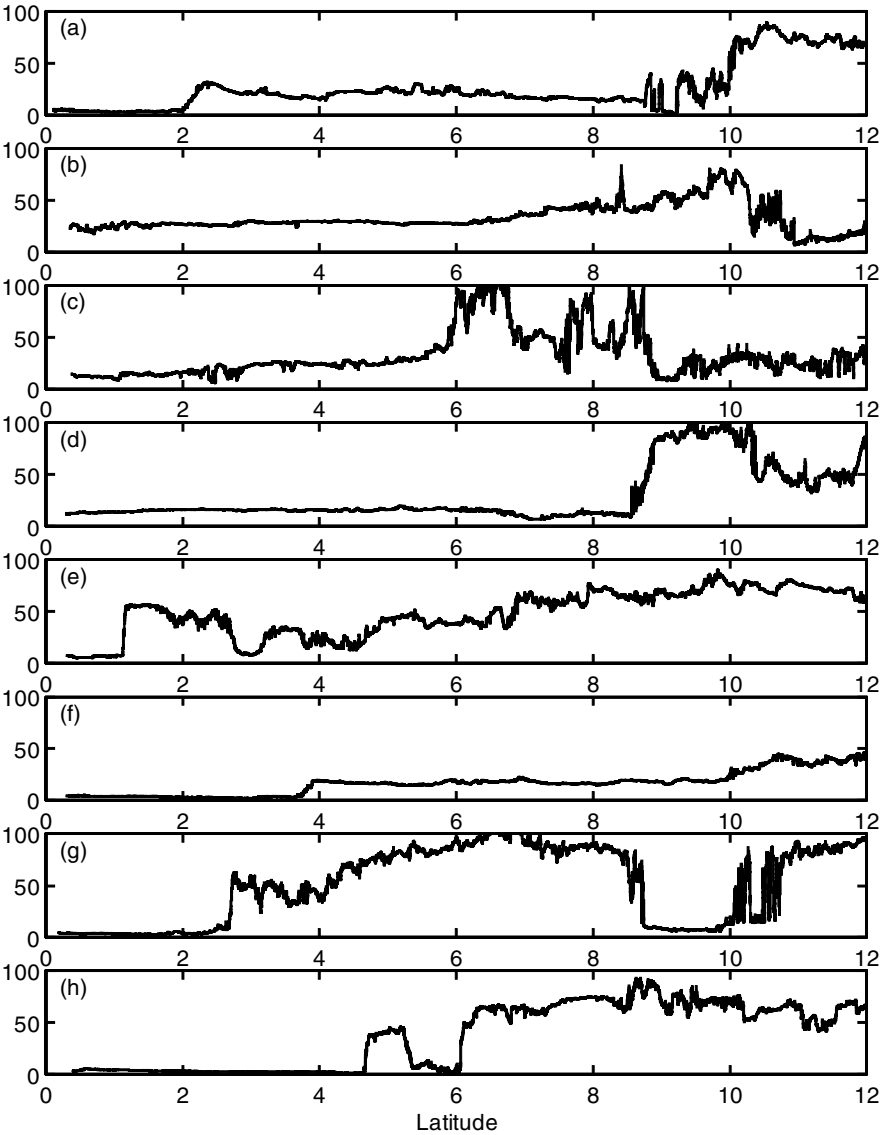

Figure 3. Flight-level 5500 m relative humidity along 95° W from the equator to 12° N measured from an aircraft during the Eastern Pacific Investigation of Climate 2001 field campaign (EPIC2001) on: (a) 7, (b) 14, (c) 19, (d) 23 and (e) 25 September, and (f) 2, (g) 9, and (h) 10 October 2001.

5. AN INTERPRETIVE FRAMEWORK

As a framework for understanding the meaning of bimodal humidity distributions, consider the following scale analysis of the relative time-scales for subsidence drying (which tends to create a dry mode by its accumulative effect, since mixing ratio is bounded below) and mixing (which tends to homogenize air properties). The existence of a moist mode consisting of regions at and near saturation is taken as a basic fact of radiative–convective equilibrium. Detailed considerations of how much condensed water these moist regions contain, and debates about the importance of that condensed

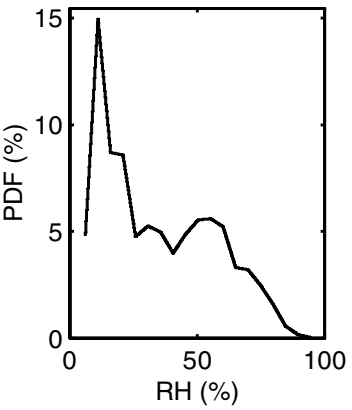

Figure 4. Estimated probability density function (PDF) of relative humidity (RH) shown in Fig. 3.

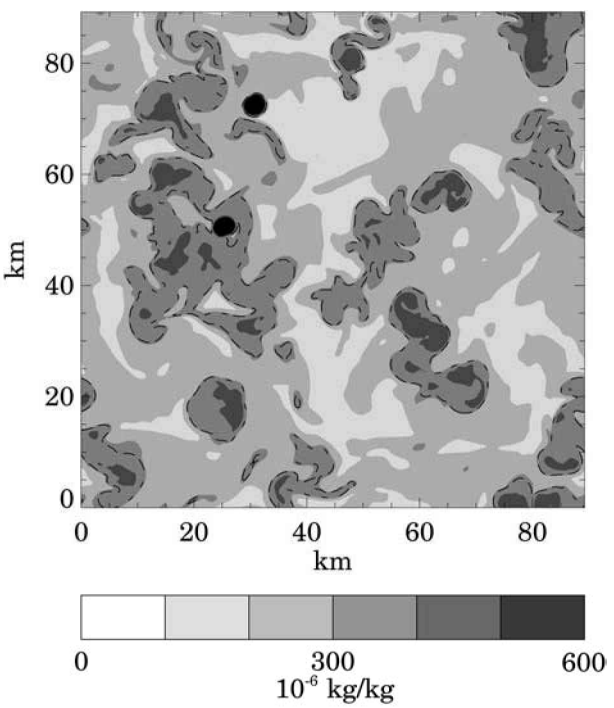

Figure 5. Humidity distribution at 10 km from a cloud-resolving model (Tompkins 2001). Dashed lines are contours of 325×10^{-6} kg kg^{-1}, which is the humidity value corresponding to the minimum probability density function between the two peaks in Fig. 6.

water to the large-scale humidity field (e.g. Sherwood 1996; Emanuel and Zivkovic-Rothman 1999; Dessler and Sherwood 2000) are beyond the scope of this study.

The lifetime of water vapour in the global and tropical troposphere is about 10 days, estimated as precipitable water (~25 mm global mean, ~35 mm tropical mean) divided by precipitation rate (~2.5 mm day^{-1} global mean, ~3.5 mm day^{-1} tropical mean). However, a more relevant time-scale at a particular altitude is the *radiative drying time*.

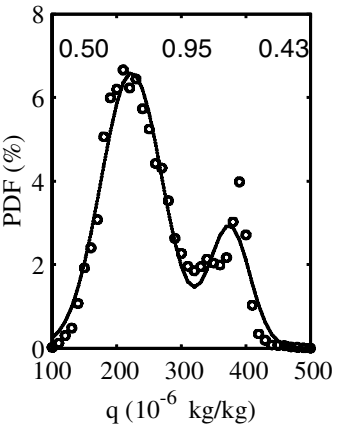

Figure 6. Estimated probability density function of relative-humidity distribution shown in Fig. 5 (circles), its best fit by normal mixtures (solid lines), and its bimodal indices (top).

The residence time of air in an atmospheric layer may be estimated as the layer thickness in potential-temperature coordinates divided by the radiative cooling rate (typically 1–2 K day^{-1} in temperature tendency units; ~1.4 times larger in potential-temperature tendency units in the upper troposphere). If the layer thickness in question is taken to be a scale height for the decrease of water vapour in the vertical, the result is a characteristic time for drying: the time for water-vapour mixing ratio to be reduced from an initial value to less than half that by radiative subsidence. The scale height for water vapour can vary widely depending on the relative-humidity profile, but for realistic radiation calculations and an initially near-saturated column this drying time is as little as 1–2 days near 10 km altitude (Mapes 2001). This short drying time is apparently the reason why bimodal humidity is preferentially found in this layer.

In order for bimodality to prevail, the characteristic time for mixing between dry and moist areas must be substantially greater than the drying time. A characteristic time for mixing can be estimated from a mixing-length approach to eddy flux convergence. Consider a dry–moist humidity difference δq, with a gradient that scales as $\delta q / L_g$, where L_g is the length-scale of the q field. The time rate of change of the difference δq due to mixing scales as the divergence of a flux, F / L_g. Suppose the flux is characterized by eddies with velocity-scale U_e and length-scale L_e. To estimate the eddy flux, multiply U_e by an eddy-scale q fluctuation, which scales as $L_e \delta q / L_g$. The resulting time-scale for the tendency of δq by eddy mixing is then: $t_m = {L_g}^2 / (U_e L_e)$

The mixing time increases as the square of the distance separating the dry and moist regions (L_g), and decreases with the size (L_e) and vigour (U_e) of eddies. This analysis is simplistic in postulating a single dominant eddy-scale, whereas true mixing requires a cascade all the way to molecular-scales (or, in more practical terms, to the scale over which our measurements are averaged). Nonetheless, it is a definite framework in which to explore the inequality of drying times and mixing times, on both the small-scales of the *in situ* and cloud-model data, and the global-scales discussed below.

Consider first the cloud-model data of Fig. 5. If $L_e = 5$ km (estimated from the curls in the humidity field), $L_g = 20$ km (estimated scale of the dry patches), and $U_e = 0.4$ m s^{-1} (the RMS wind velocity at this level), then t_m is 2.3 days. This is greater than the radiative drying time (from Fig. 1 of Mapes 2001) only in the layer near 10 km altitude, which is indeed the only place where bimodality is observed in the model output.

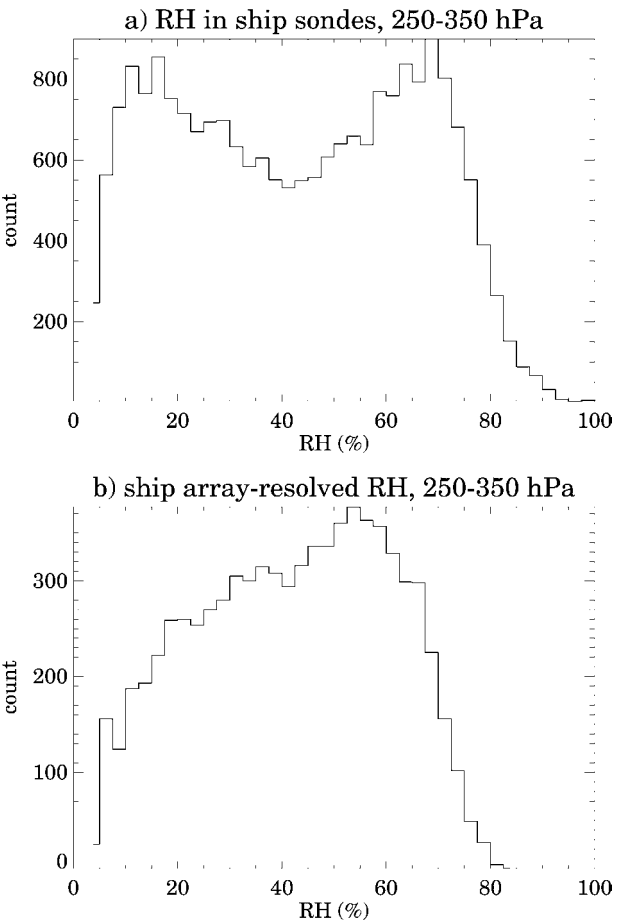

Figure 7. Estimated probability density functions (PDFs, *y*-axis) of: (a) relative humidity (RH) in 6-hourly 5 hPa samples in all radiosonde data from four TOGA COARE (see subsection 2(a)) ships in the layer between 250 and 350 hPa; (b) PDFs of RH averaged over the four ship soundings at each 6-hour nominal sounding time, and further smoothed by a three-point running mean in time.

6. Larger scales

Averaging acts like a powerful form of mixing; time averages of the cloud-model humidity fields, for example, rapidly approach uniformity in space. The Central Limit Theorem states that the sum of a large number of independent identically distributed variables will approach a unimodal (Gaussian) distribution, even if those variables have a bimodal distribution. As a result, the bimodality seen in section 5 in point samples tends to disappear in lower-resolution data created by space and time averaging.

Figure 7(a) shows the bimodal distribution of relative humidity in 6-hourly, 5 hPa samples in all radiosonde data from the four COARE ships in the layer between 250–350 hPa. These ships were stationed within a few hundred kilometres of each other, and most of the variability they sampled is on larger scales, including a major contribution from the planetary-scale intraseasonal oscillation. The variability on space- and time-scales large enough to be resolved by the radiosonde array, of which the ships formed an especially dense part, has been isolated by averaging all the data available at the four ship sites and at each 6-hour nominal sounding time, and further smoothing

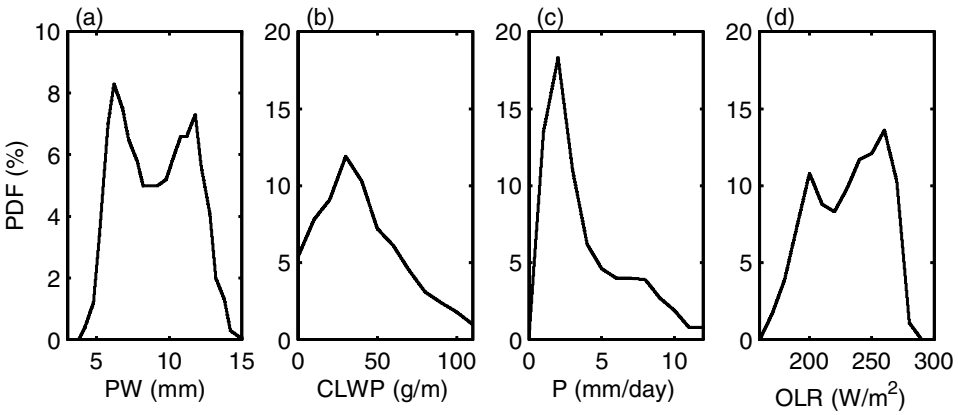

Figure 8. Estimated probability density functions of: (a) NASA Water Vapor Project (NVAP) 500–300 hPa precipitable water, (b) Special Sensor Microwave/Imager (SSM/I) cloud-water liquid path, (c) National Oceanic and Atmospheric Administration Climate Prediction Center Merged Analysis of Precipitation (CMAP) precipitation rate, and (d) outgoing long-wave radiation. All are for climatologically mean January from 20° N to 20° S. See text for further details.

the data with a three-point running mean in time. The distribution of this 'large-scale' or well-resolved component of the variability is shown in Fig. 7(b). Although the range and variance are not drastically smaller than in Fig. 7(a), the bimodality is gone and, in particular, the dry mode at <20% is essentially gone. This suggests that the very dry air in this climatologically convective region occurs in pockets smaller than the averaging-scales (a few hundred km, 18 h).

The next appearance of bimodal tropospheric humidity comes at planetary-scales, with the western Pacific warm pool tending to be a moist region in monthly mean data. Figure 8(a) shows a PDF for precipitable water in the mid-troposphere (500–300 hPa) and in a global tropical region, 20°N–20°S, estimated from satellite remote sensing (subsection 2(h)). Its bimodality is unmistakable. Because the main sources of tropospheric water vapour are deep convective updraughts, one may expect that a global-scale bimodal PDF of tropical water vapour exists simply because the convective cloud fraction is bimodal. This is, however, not necessarily true. A bimodal PDF of water vapour can exist when PDFs of cloud liquid-water path and precipitation are unimodal (Figs. 8(b) and (c)), without any peak corresponding to the source region. Bimodality indeed appears in OLR, which measures both water vapour and cloud (Fig. 8(d)). The bimodal PDF in Fig. 8(a) is unlikely to be caused by the non-uniform distribution of data sources (see subsection 2(h)). It still exists when data from a single source (satellite over ocean) are used. Planetary-scale bimodality also exists in other water-vapour products of satellite remote sensing (e.g. SSMR, not shown).

Bimodality at this global scale survives despite the strong mixing implied by monthly averaging (and even climatological monthly averaging), because of the spatial separation of moist and dry areas on scales much larger than the grid-scale of global products (1–2.5 degrees). This spatial separation of regions with and without deep convective moisture sources reflects large-scale structure in the land–sea distribution on earth and the concomitant sea surface temperature structure, with vast cold regions in the eastern Atlantic and Pacific basins. At this global spatial scale, horizontal mixing is carried out by synoptic eddies and aided by our monthly time averaging. Turning again to the scale analysis above, if a bimodal distribution requires $t_m > 2$ days then this

TABLE 2. BIMODAL AMPLITUDE (A_B), BIMODAL SEPARATION (S), AND BIMODAL RATIO (R) FOR CLIMATOLOGICAL MONTHLY MEAN NASA WATER VAPOR PROJECT PRECIPITABLE WATER FROM 20°N TO 20°S.

	Jan	Feb	Mar	Apr	May	Jun	Jul	Aug	Sept	Oct	Nov	Dec
						750–500 hPa						
A_B	***0.41***	***0.40***	***0.41***	0.06	*0.17*	***0.16***	*0.22*	*0.28*	0.12	0.14	*0.09*	***0.32***
S	***0.78***	***0.76***	***0.78***	0.48	*0.63*	***0.64***	*0.71*	*0.74*	0.66	0.60	*0.44*	***0.74***
R	***0.89***	***0.85***	***1.17***	0.63	*0.97*	***0.97***	*1.20*	*1.26*	1.25	1.16	*0.66*	***1.10***
						500–300 hPa						
A_B	***0.23***	***0.36***	***0.37***	0	***0.19***	*0.09*	***0.28***	***0.37***	***0.31***	*0.18*	0.06	***0.24***
S	***0.66***	***0.61***	***0.69***	0.57	***0.66***	*0.66*	***0.67***	***0.72***	***0.61***	*0.67*	0.51	***0.63***
R	***0.89***	***0.85***	***1.13***	1.08	***0.96***	*1.09*	***1.09***	***1.04***	***1.40***	*1.11*	0.76	***1.20***

Numbers in italics indicate two peaks are visually detected from estimated PDFs; bold numbers indicate that bimodality is confirmed by rejecting hypothesis H_0 (see text) at the 95% confidence level.

implies $L_g > (2U_eL_e)^{1/2}$. If $U_e \sim 10$ m s^{-1} and $L_e \sim 2000$ km, then L_g (the scale of moist and dry regions) must exceed ~2000 km.

A similar scaling is reached if $u\,\mathrm{d}q/\mathrm{d}x$ (where u is the wind speed) rather than an eddy flux divergence is used to define the mixing time (in that case perhaps a better name would be 'smearing time'). The study of Pierrehumbert and Roca (1998) demonstrates that both time-mean flow and synoptic-scale transient eddies are important in determining the humidity of the subtropical dry zones.

On earth, the large-scale patterns of convection and subtropical dry zones tend to exceed this critical size, although these patterns undergo seasonal cycles. Bimodality in water vapour indeed varies annually in climatological monthly mean spatial distributions of water vapour, and exists in the annual cycle of water vapour. Table 2 lists the bimodal indices defined in section 3 for monthly mean spatial variability of PW in the middle (750–500 hPa) and upper (500–300 hPa) troposphere. There is no bimodality in the lower troposphere (1000–750 hPa), as can be seen in Fig. 2. The seasonality in bimodality is apparent: it is weak or absent in boreal spring and fall, and strong in boreal summer and winter. This semi-annual signal in bimodality might be related to the semi-annual cycles in tropical deep convection and circulation (e.g. Weikmann and Chervin 1988). Large-scale mixing might be relatively more efficient to smear sharp gradients in water vapour when its deep convective sources are relatively weak.

Bimodality in the local, temporal variability associated with the annual cycle of PW exists only in confined regions (Fig. 9). Most of them are close to or over the continents, some are associated with the monsoons. It is interesting to point out that the bimodality in the annual cycle of tropospheric water vapour does not necessarily depend on the strength of the annual cycle of water vapour itself. The areas of prominent bimodality in the annual cycle (for instance in Fig. 9(b)) are not always collocated with the areas of large amplitude of the annual cycle in PW (Fig. 9(d)); the eastern Pacific is a case in point. The strongest annual cycle in PW is seen in the North American monsoon region (the Pacific coast of Mexico and the south-western USA), whereas the most prominent bimodal signals are found either east of this in the Caribbean Sea, or south over the eastern Pacific cold tongue. The bimodality in the annual cycle implies fast transition between lasting dry and moist (rainy) seasons. This again indicates that the drying processes after the rainy season are far more efficient (with a shorter time-scale) than mixing.

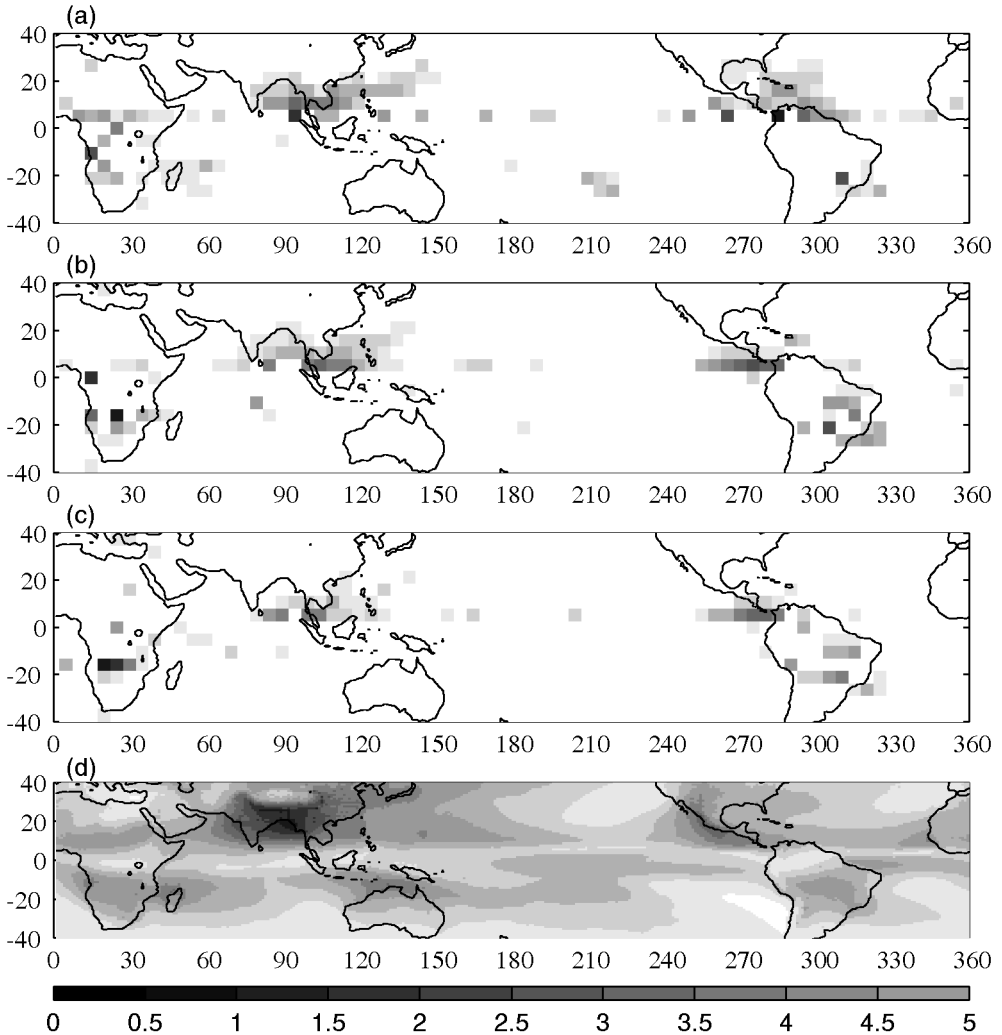

Figure 9. Areas of bimodal probability density functions indicated by shading, for the annual cycle in NASA Water Vapor Project (NVAP) precipitable water (PW) from: (a) the surface to 750 hPa, (b) 750 to 500 hPa, and (c) 500 to 300 hPa. (d) Standard deviation of the annual cycle of 750–500 hPa NVAP PW calculated using deviations from each year's annual mean. Darker shading indicates larger amplitude of the annual cycle.

7. Discussion

In this study, we have:

(i) introduced a method of testing for and quantifying bimodal PDFs;
(ii) demonstrated that bimodality exists in tropical water vapour in a variety of regions and different time-scales; and
(iii) related the observed bimodality to atmospheric mixing processes.

Bimodality in tropical water vapour is an interesting issue because of its potential implications regarding the water-vapour feedback to climate, and the ability of reproducing and predicting the water-vapour distribution in state-of-the-art global models.

Because the absorptivity of water vapour increases roughly logarithmically with its concentration, the effect on the OLR of water vapour at any particular altitude depends

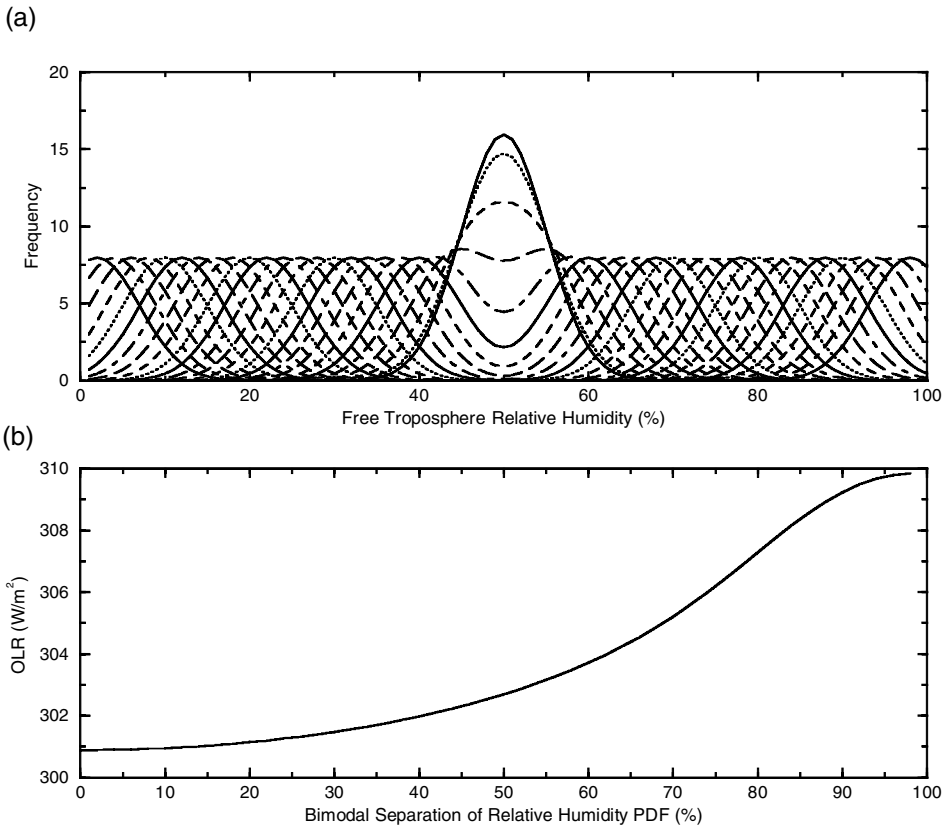

Figure 10. (a) Probability density functions (PDFs) of an idealized vertically-invariant relative humidity (RH) profile, for which the mean RH is held constant at a value of 50%. (b) Mean clear-sky outgoing long-wave radiation (OLR) for each PDF as a function of modal separation.

upon its mean concentration (averaged over a given time or spatial domain) as well as the variation of its distribution about that mean. To illustrate this, we performed idealized calculations of OLR using a standard tropical temperature profile and a constant RH profile in the vertical. Over the free troposphere (defined here as 800–200 hPa) the value of the vertically invariant RH is increased from 1% to 100% and the resulting clear-sky OLR is computed using the National Center for Atmospheric Research (NCAR) Community Climate System Model (CCSM3) single-column radiation code (Kiehl and Briegleb 1993). Consider a range of PDFs of the vertically-invariant RH profile (Fig. 10(a)). The mean RH is held constant at a value of 50%, but the distribution is allowed to vary by the formation of bimodal PDFs with modes that diverge from zero (i.e. a unimodal Gaussian PDF) to 99% (i.e. an extreme bimodal distribution with mode peaks near 1% and 100% RH). We then calculated the corresponding mean clear-sky OLR for each PDF, which is plotted as a function of modal separation (Fig. 10(b)). Note that for a given mean RH, the mean OLR increases systematically as the bimodality (or variance) of the PDF increases, again reflecting the logarithmic dependence of the absorptivity on the water-vapour concentration. Thus, even if the mean RH remains unchanged, a shift in its distribution can have a significant effect (up to 10 W m^{-2}) on mean OLR. Such an effect is comparable to what would be obtained by a systematic change in the water vapour concentration by $\sim$20% under standard tropical conditions.

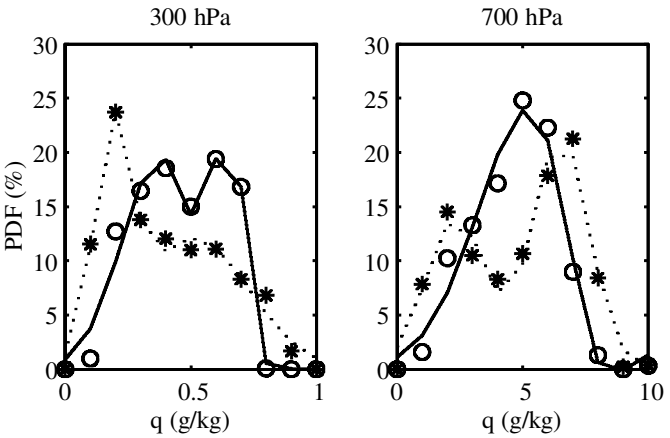

Figure 11. Estimated probability density functions of specific humidity (q) at 300 and 700 hPa from the NCEP/NCAR re-analysis (circles) and a CCSM simulation (asterisks) for the climatological mean for January in the tropics (20°N–20°S). Curves are best normal mixture fits. See text for details.

This effect of the bimodality on OLR is through the changes in the variance of the water-vapour distribution.

As briefly discussed in the introduction, there is no obvious reason for tropical water vapour to be bimodal. A coexistence of extreme dry and moist regimes does not necessarily lead to bimodality. Bimodality exists possibly only when drying time is shorter than mixing time. Physical processes responsible for the observed bimodality are not always well represented in global models. PDFs of tropical (20°N–20°S) water vapour from the NCEP/NCAR re-analysis (Kalnay *et al.* 1996) and a simulation of the NCAR CCSM (Blackmon *et al.* 2001) are compared in Fig. 11 for the climatological mean of January. Here by no means do we view the water-vapour distribution in the re-analysis as reality. It is interesting to see that in the upper troposphere (300 hPa) bimodality exists in the re-analysis but is absent from the model simulation. By contrast, in the lower troposphere (700 hPa) bimodality exists in the model simulation but is absent from the re-analysis. It is not known whether the discrepancies are caused by the differences in model physics or as a consequence of data assimilation in the re-analysis. There are, however, not many observations of water vapour in the tropics available for the re-analysis. This comparison suggests that the reproduction of the bimodality of water vapour is model dependent. In conclusion, we suggest that the observed bimodality of water vapour reveals aspects of the atmospheric dynamics and may serve as a simple but sensitive statistical discriminator of model treatment of water vapour.

Acknowledgements

This study was supported by NSF Grant ATM-0070703 (CZ and BEM) and DOE/ARM Grant DE-AI02-00ER62900 (BJS).

Appendix

Testing for bimodality

Testing for bimodality or, more generally, for multimodality, of a PDF involves two steps: estimating the PDF and rejecting the hypothesis of unimodality. These two steps

can in some cases be combined into one. In many applications, however, the main focus is on the first step: estimating PDFs. It is very common that once a PDF is estimated and tested, it is taken to be bimodal as long as it shows two peaks (e.g. Hansen and Sutera 1986).

But having a best estimate of a PDF that shows two peaks is one thing, and proving it is truly bimodal is quite another. The key problem is not only whether any two peaks in an estimated PDF may result from insufficient sampling or inappropriate parameters (such as the bin width of histograms), but also simply by chance. These factors can be addressed by many existing methods of estimating PDFs. The key problem is whether an appropriately estimated PDF with two peaks always represents bimodality.

There exist a number of methods of testing for multimodality (see Hartigan and Hartigan (1985) and Silverman (1986) for brief summaries). Most of them, however, involve parameters that need to be given a priori or to be tuned to achieve the best result.

A 'dip test' for multimodality was proposed by Hartigan and Hartigan (1985) and coded by Hartigan (1985). It calculates departure of a sample from unimodality. This method is non-parametric. It estimates the maximum difference between the empirical distribution function $F_n(x)$ and the unimodal distribution function $F(x)$ that minimizes that maximum difference:

$$DIP = \min_{F \in U} \left\{ \sup_x |F_n(x) - F(x)| \right\}, \tag{A.1}$$

where U is the class of all unimodal distribution functions. *DIP* asymptotically approaches zero for samples from a unimodal distribution, and a positive constant for samples from any multimodal distribution. The main advantage of the dip test over other methods is that it does not depend on estimated PDFs. Therefore, no a priori assumption is required, such as the bin width for estimating PDFs using the histogram method and the kernel width using the kernel method (Silverman 1986). The dip test is designed to test the hypothesis that the given samples are from a unimodal distribution. Rejecting this hypothesis indicates multimodality. The method cannot, however, directly determine the number of the modes when the unimodality hypothesis is rejected. It, nonetheless, provides an objective way to formally confirm bimodality when an estimated PDF shows two peaks.

REFERENCES

Bates, J. J. and Jackson, D. L. 1997 A comparison of water vapor observations with AMIP I simulations. *J. Geophys. Res.*, **102,** 21837–21852

Blackmon, M., Boville, B., Bryan, F., Dickinson, R., Gent, P., Kiehl, J., Moritz, R., Randall, D., Shukla, J., Solomon, S., Bonan, G., Doney, S., Fung, I., Hack, J., Hunke, E., Hurrell, J., Kutzbach, J., Meehl, J., Otto-Bliesner, B., Saravanan, R., Schneider, E. K., Sloan, L., Spall, M., Taylor, K., Tribbia, J. and Washington, W. 2001 The Community Climate System Model. *Bull. Am. Meteorol. Soc.*, **82,** 2357–2376

Broecker, W. S. 1997 Mountain glaciers: Recorders of atmospheric water vapor content? *Global Biogeochem. Cycles*, **11,** 589–597

Brown, R. G. and Zhang, C. 1997 Variability of mid-tropospheric humidity and its effect on cloud-top height distribution during TOGA COARE. *J. Atmos. Sci.*, **54,** 2760–2774

Cho, J. Y. N., Newell, R. E. and Sachse, G. W. 2000 Anomalous scaling of mesoscale tropospheric humidity fluctuations. *Geophys. Res. Lett.*, **27,** 377–380

Dessler, A. E. and Sherwood, S. C. 2000 Simulations of tropical upper tropospheric humidity. *J. Geophys. Res.*, **105,** 20155–20163

Emanuel, K. E. and Zivkovic-Rothman, M. 1999 Development and evaluation of a convection scheme for use in climate models. *J. Atmos. Sci.*, **56,** 1766–1782

Hansen, A. R. and Sutera, A. 1986 On the probability density distribution of planetary-scale atmospheric wave amplitude. *J. Atmos. Sci.*, **43,** 3250–3265

Hartigan, P. M. 1985 Computation of the dip statistics to test for unimodality. *Appl. Stat.*, **34,** 320–325

Hartigan, J. A. and Hartigan, P. M. 1985 The dip test of unimodality. *Ann. Stat.*, **13,** 70–84

Held, I. M. and Soden, B. J. 2000 Water vapor feedback and global warming. *Ann. Rev. Energy Environ.*, **25,** 441–475

IPCC 2000 *Emissions scenarios*. Cambridge University Press, London, UK
2001 *Climate change*: *Synthesis report*. Cambridge University Press, London, UK

Kalnay, E. M., Kanamitsu, M., Kistler, R., Collins, W., Deaven, D., Gandin, L., Iredell, M., Saha, S., White, G., Woollen, J., Zhu, Y., Leetmaa, A., Reynolds, B., Chelliah, M., Ebisuzaki, W., Higgins, W., Janowiak, J., Mo, K. C., Ropelewski, C., Wang, J., Jenne, R. and Joseph, D. 1996 NCEP/NCAR 40-year reanalysis project. *Bull. Am. Meteorol. Soc.*, **77,** 437–471

Kiehl, J. T. and Briegleb, B. P. 1993 The radiative roles of sulfate aerosols and greenhouse gases in climate forcing. *Science*, **260,** 311–314

Kley, D., Smit, H. G. J., Vomel, H., Grassl, H., Ramanathan, V., Crutzen, P. J., Williams, S., Meywerk J. and Oltmans S. J. 1997 Tropospheric water-vapour and ozone cross-sections in a zonal plane over the central equatorial Pacific Ocean. *Q. J. R. Meteorol. Soc.*, **123,** 2009–2040

Kloesel, K. A. and Albrecht, B. A. 1989 Low-level inversions over the tropical Pacific—thermodynamic structure of the boundary layer and the above-inversion moisture structure. *Mon. Weather Rev.*, **117,** 87–101

Liebmann, B. and Smith C. A. 1996 Description of a complete (interpolated) outgoing long-wave radiation dataset. *Bull. Am. Meteorol. Soc.*, **77,** 1275–1277

Lohmann, U., Roeckner, E., Collins, W. D., Heymsfield, A. J., McFarquhar, G. M. and Barnett, T. P. 1995 The role of water vapor and convection during the Central Equatorial Pacific Experiment (CEPEX) from observations and model simulations. *J. Geophys. Res.–Atmos.*, **100,** 26229–26246

Mapes, B. E. 2001 Water's two height scales: the moist adiabat and the radiative troposphere. *Q. J. R. Meteorol. Soc.*, **127,** 2253–2266

Mapes, B. E. and Zuidema, P. 1996 Radiative and dynamical consequences of dry tongues in the tropical troposphere. *J. Atmos. Sci.*, **53,** 620–638

Mather, J. H., Ackerman, T. P., Clements, W. E., Barnes, F. J., Ivey, M. D., Hatfield, L. D. and Reynolds. R. M. 1998 An atmospheric radiation and cloud station in the tropical western Pacific. *Bull. Am. Meteorol. Soc.*, **79,** 627–642

Newell, R. E. and Gould-Stewart, S. 1981 A stratospheric fountain? *J. Atmos. Sci.*, **38,** 2789–2796

Panofsky, H. A. and Brier, G. W. 1958 *Some applications of statistics to meteorology*. The Pennsylvania State University, College, USA

Pierrehumbert, R. T. and Roca, R. 1998 Evidence for control of subtropical Atlantic humidity by large-scale advection. *Geophys. Res. Lett.*, **25,** 4537–4540.

Randel, D. L., Greenwald, T. J., Vonder Haar, T. H., Stephens, G. L., Ringerud, M. A. and Combs, C. L. 1996 A new global water vapor data set. *Bull. Am. Meteorol. Soc.*, **77,** 1233–1246

Reschenhofer, E. 2001 The bimodality principle. *J. Stat. Educ.*, **9,** 1

Sherwood, S. C. 1996 Maintenance of the free-tropospheric tropical water vapor distribution. Part I: Clear regime budget. *J. Climate*, **9,** 2903–2918
1999 Convective precursors and predictability in the tropical western Pacific. *Mon. Weather Rev.*, **127,** 2977–2991
2000 A stratospheric 'drain' over the maritime continent. *Geophys. Res. Lett.*, **27,** 677–680

Silverman, B. W. 1986 *Density estimation for statistics and data analysis*. Chapman and Hall, London, UK

Soden, B. J. and Bretherton, F. P. 1993 Upper tropospheric relative humidity from the GOES 6.7 μm channel: Method and climatology for July 1987. *J. Geophys. Res.*, **98,** 16669–16688

Tompkins, A. 2001 Organization of tropical convection in low vertical wind shears: The role of water vapor. *J. Atmos. Sci.*, **58,** 529–545

Wang, J., Cole, H. L., Carlson, D. J., Miller, E. R., and Beierle, K., Paukkunen, A. and Laine, T. K. 2002 Corrections of humidity measurement errors from the Vaisala RS80 radiosonde—application to TOGA COARE data. *J. Atmos. Oceanic Technol.*, **19,** 981–1002

Webster, P. J. and Lukas, R. 1992 TOGA COARE: The Coupled Ocean–Atmosphere Response Experiment. *Bull. Am. Meteorol. Soc.*, **73,** 1377–1416

Webster, P. J., Bradley, E. F., Fairall, C. W., Godfrey, J. S., Hacker, P., Houze, R. A. Jr., Lukas, R., Serra, Y., Hummon, J. M., Lawrence, T. D. M., Russell, C. A., Ryan, M. N., Sahami, K. and Zuidema, P. 2002 The JASMINE pilot study. *Bull. Am. Meteorol. Soc.*, **83,** 1603–1630

Weickmann, K. M. and Chervin, R. M. 1988 The observed and simulated atmospheric seasonal cycle. Part I: Global wind field modes. *J. Climate*, **1,** 265–289

Weller, B. 1999 A science and implementation plan for EPIC: An eastern Pacific investigation of climate processes in the coupled ocean–atmosphere system. Available at http://www.atmos.washington.edu/gcg/EPIC

Weng, F. and Grody, N. C. 1994 Retrieval of cloud liquid water using the Special Sensor Microwave Imager. *J. Geophys. Res.*, **99,** 14493–14502

Xie, P. and Arkin, P. A. 1997 Global precipitation: A 17-year monthly analysis based on gauge observations, satellite estimates, and numerical model output. *Bull. Am. Meteorol. Soc.*, **78,** 2539–2358

Yang, H. and Pierrehumbert, R. T. 1994 Production of dry air by isentropic mixing. *J. Atmos. Sci.*, **51,** 3437–3454

Yin, B. and Albrecht, B. A. 2000 Spatial variability of atmospheric boundary layer structure over the eastern equatorial Pacific. *J. Climate*, **13,** 1574–1592

Yoneyma, K. and Parsons, D. B. 1999 A proposed mechanism for the intrusion of dry air into the tropical western Pacific region. *J. Atmos. Sci.*, **56,** 1524–1546

Yuter, S. E. and Houze, R. A. Jr. 2000 The 1997 Pan American Climate Studies Tropical Eastern Pacific Process Study. Part I: ITCZ region. *Bull. Am. Meteorol. Soc.*, **81,** 451–481

Zhang, C. and Chou, M.-D. 1999 Variability of water vapor, infrared radiative cooling, and for convection in the western Pacific. *J. Atmos. Sci.*, **56,** 711–723